# Phase Equilibria in the Mo−Fe−P System at 800 °C and Structure of Ternary Phosphide $(Mo_{1-x}Fe_x)_3P$ $(0.10 \leq x \leq 0.15)$

Anton O. Oliynyk,[†,‡] Yaroslava F. Lomnytska,*[,‡] Mariya V. Dzevenko,[‡] Stanislav S. Stoyko,[†] and Arthur Mar*[,†]

[†]Department of Chemistry, University of Alberta, Edmonton, Alberta, Canada T6G 2G2
[‡]Department of Analytical Chemistry, Ivan Franko National University of Lviv, 79005 Lviv, Ukraine

Ⓢ *Supporting Information*

ABSTRACT: Construction of the isothermal section in the metal-rich portion (<67 atom % P) of the Mo−Fe−P phase diagram at 800 °C has led to the identification of two new ternary phases: $(Mo_{1-x}Fe_x)_2P$ ($x = 0.30-0.82$) and $(Mo_{1-x}Fe_x)_3P$ ($x = 0.10-0.15$). The occurrence of a Co_2Si-type ternary phase $(Mo_{1-x}Fe_x)_2P$, which straddles the equiatomic composition MoFeP, is common to other ternary transition-metal phosphide systems. However, the ternary phase $(Mo_{1-x}Fe_x)_3P$ is unusual because it is distinct from the binary phase Mo_3P, notwithstanding their similar compositions and structures. The relationship has been clarified through single-crystal X-ray diffraction studies on Mo_3P (α-V_3S-type, space group $I\bar{4}2m$, $a = 9.7925(11)$ Å, $c = 4.8246(6)$ Å) and $(Mo_{0.85}Fe_{0.15})_3P$ (Ni_3P-type, space group $I\bar{4}$, $a = 9.6982(8)$ Å, $c = 4.7590(4)$ Å) at −100 °C. Representation in terms of nets containing fused triangles provides a pathway to transform these closely related structures through twisting. Band structure calculations support the adoption of these structure types and the site preference of Fe atoms. Electrical resistivity measurements on $(Mo_{0.85}Fe_{0.15})_3P$ reveal metallic behavior but no superconducting transition.
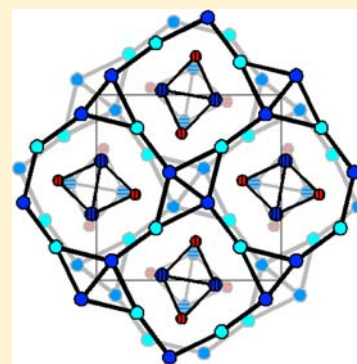
■ INTRODUCTION

Much of the current interest in transition-metal phosphides, especially metal-rich binary phases such as Ni_2P, lies in their potential as hydroprocessing catalysts for petroleum upgrading.[1] However, transition-metal phosphides exhibit diverse structures, bonding, and properties that deserve further investigation. The recent discovery of many new iron-based pnictide superconductors (largely based on the $ThCr_2Si_2$-type structure)[2,3] led us to inquire whether other previously known phosphides may be worth re-examining. In this regard, the binary Mo−P system elicits attention because it contains several superconducting phases, including Mo_3P, which has the highest transition temperature ($T_c = 7.0$ K) found among binary phosphides.[4] The transition temperature increases to 15.5 K in the ternary phosphides MoNiP and MoRuP.[5] It has been speculated that Mo−Mo bonding, which corresponds to quite short distances in the metal-rich Mo-containing phases, plays an important role in the development of superconductivity in these compounds.[4,5] There remains some ambiguity in the structure of Mo_3P itself, which was inferred earlier from powder X-ray diffraction data and later determined through single-crystal photographic methods only.[6−8]

Previous investigations of phase equilibria in ternary Mo−M′−P systems have been limited to M′ = Ti, Fe, Ni.[9−11] In the Mo−Fe−P system, no complete phase diagram is available, and the existence of ternary phases has been established only for MoFeP (TiNiSi-type) and $MoFe_2P_{12}$ (own type).[12,13] We report here the construction of the metal-rich portion (<67 atom % P) of the Mo−Fe−P phase diagram at 800 °C in which

the ternary phases $(Mo_{1-x}Fe_x)_2P$ and $(Mo_{1-x}Fe_x)_3P$ have been identified. Interestingly, $(Mo_{1-x}Fe_x)_3P$ is formed *not* merely through a substitutional solid solution as an extension of the binary phase Mo_3P, but rather it adopts a subtly different structure type. We seek rationalization of these differences by analyzing the bonding through band structure calculations. The electrical resistivity of one member of $(Mo_{1-x}Fe_x)_3P$ ($x = 0.15$) was also measured.

■ EXPERIMENTAL SECTION

Synthesis. Samples were prepared from mixtures of Mo, Fe, and P powders, each of purity greater than 99.9%, which were pressed into pellets and subjected to appropriate heat treatment depending on the phosphorus content. For samples with less than 20 atom % P, the mixtures were reacted directly in an electric arc melter under an argon atmosphere. For samples with 20−35 atom % P, the mixtures were placed within evacuated fused-silica tubes which were heated from 20 to 800 °C over 2 h, kept at 800 °C over 5−7 days, and then cooled to room temperature by shutting off the furnace. The sintered pellets were ground, pressed again into pellets, and arc-melted. For samples with greater than 35 atom % P, the mixtures were reacted within evacuated fused-silica tubes as above but at a much slower heating rate, from 20 to 800 °C over 8 days, to minimize volatilization of phosphorus and with a longer holding time at 800 °C for 8 days. The sintered pellets were ground and pressed again into pellets, but no subsequent arc-melting was applied. In all three cases, the samples were further annealed within evacuated fused-silica tubes at 800 °C for

1 month, followed by quenching in cold water. The final weights of the annealed samples did not deviate from the initial weights of the unreacted mixtures by more than 2%.

Phase Analysis. The phase compositions of the products were largely determined through powder X-ray diffraction patterns collected with Cu Kα radiation on a DRON-3 M diffractometer or with Cu Kα_1 radiation on a STOE STADI P (transmission mode) or an Inel CPS-120 diffractometer. Cell parameters for phases were refined from the powder diffraction data with use of the CSD suite of programs.[14] Homogeneity ranges for solid solutions were established through analysis of the powder X-ray diffraction (XRD) patterns, by noting the presence of single-phase vs multiphase regions as a function of composition and identifying breaks in the lattice parameter trends. We estimate the uncertainty of the solid solubility limits to be ±(0.01−0.02) in x, depending on the phase.

To ascertain the solubility of the third component in binary phases, their cell parameters obtained from products of three-component samples were compared to those of the pure phases. For example, MoP$_2$ (own type, space group $Cmc2_1$) was found to solubilize a small amount of Fe, as deduced from the slight contraction in cell parameters from a = 3.1415(6) Å, b = 11.174(2) Å, and c = 4.9793(8) Å in the parent binary phase to a = 3.140(1) Å, b = 11.157(3) Å, and c = 4.977(1) Å in the limiting end-member Mo$_{0.9}$Fe$_{0.1}$P$_2$. Fe$_3$P (Ni$_3$P-type, space group $I\bar{4}$) solubilizes a small amount of Mo, as seen by the slight expansion in cell parameters from a = 9.107(5) Å, c = 4.460(5) Å in the parent binary phase to a = 9.118(6) Å, c = 4.469(5) Å in the limiting end-member (Fe$_{0.93}$Mo$_{0.07}$)$_3$P.[15] From other similar observations, it was confirmed that MoP and Fe$_2$P support slight solubility of the third component,[16−18] whereas all remaining binary phases (Mo$_3$P, Mo$_4$P$_3$, FeP, FeP$_2$, Mo$_6$Fe$_7$, and MoFe$_2$) have negligible solubility of the third component.

The analysis of the powder diffraction data revealed the existence of two ternary phases, (Mo$_{1−x}$Fe$_x$)$_2$P (Co$_2$Si-type) and (Mo$_{1−x}$Fe$_x$)$_3$P (Ni$_3$P-type). The homogeneity ranges of these ternary phases were determined by identifying the compositions where single-phase products were obtained for samples at the 33 and 25 atom % P sections for (Mo$_{1−x}$Fe$_x$)$_2$P and (Mo$_{1−x}$Fe$_x$)$_3$P, respectively. Plots of the cell parameters indicate that the homogeneity range is quite wide for (Mo$_{1−x}$Fe$_x$)$_2$P (x = 0.30−0.82) but narrow for (Mo$_{1−x}$Fe$_x$)$_3$P (x = 0.10−0.15) (Figure 1).

Structure Determination of Mo$_3$P and (Mo$_{1−x}$Fe$_x$)$_3$P. From the results above, it became important to rule out the possibility that (Mo$_{1−x}$Fe$_x$)$_3$P (x = 0.10−0.15) is not just a simple extension of the binary phase Mo$_3$P, given their similarities in composition, cell parameters, and crystal system. Metallographic analysis was performed on a two-phase sample which was polished, embedded in resin, and examined on a JEOL JSM-6010LA scanning electron microscope. The backscattered electron image reveals that darker regions of the ternary phase (Mo$_{1−x}$Fe$_x$)$_3$P can be distinguished from brighter regions of the binary phase Mo$_3$P (Figure S1 in Supporting Information). As determined from energy-dispersive X-ray (EDX) analysis, the average elemental composition of the ternary phase is close to that expected for the lower limit of Fe substitution, (Mo$_{0.90}$Fe$_{0.10}$)$_3$P. The powder X-ray diffraction patterns for these two phases are also similar, but they can be deconvoluted as two separate sets in the experimental pattern, which was refined with the Rietveld method using the FullProf program package (Figure 2).[19] Given the complexity of this pattern, only an overall temperature factor could be introduced for each phase, and refinement of the occupancies of the disordered Mo/Fe site in the ternary phase was not possible. Table 1 summarizes crystallographic details of this refinement.

Firmer evidence for the distinction between Mo$_3$P and (Mo$_{1−x}$Fe$_x$)$_3$P was sought through single-crystal X-ray diffraction data. Because the earlier structural investigation of Mo$_3$P was based only on photographic data,[8] a redetermination based on diffractometer data was deemed to be worthwhile. A single crystal of Mo$_3$P was selected from the preparation of this binary phase, whereas a single crystal of (Mo$_{1−x}$Fe$_x$)$_3$P was selected from a three-phase sample in which the composition of this ternary phase should correspond to the upper limit of Fe substitution, (Mo$_{0.85}$Fe$_{0.15}$)$_3$P. The compositions of

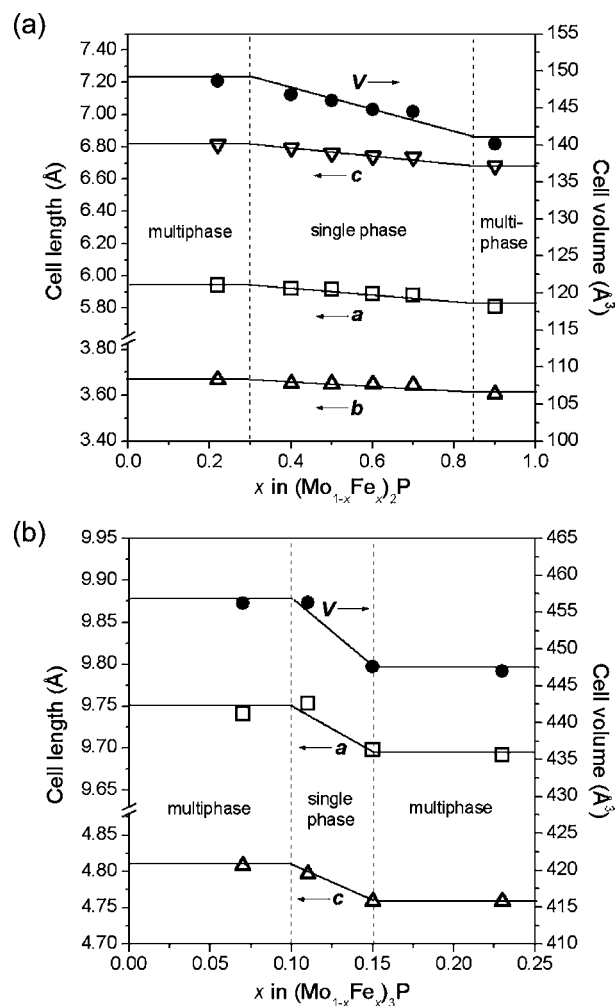**Figure 1.** Plots of cell parameters vs x for (a) (Mo$_{1−x}$Fe$_x$)$_2$P (Co$_2$Si-type) and (b) (Mo$_{1−x}$Fe$_x$)$_3$P (Ni$_3$P-type) phases observed in reactions with the nominal compositions indicated. The uncertainties in the cell parameters and in x are on the order of the symbol sizes.
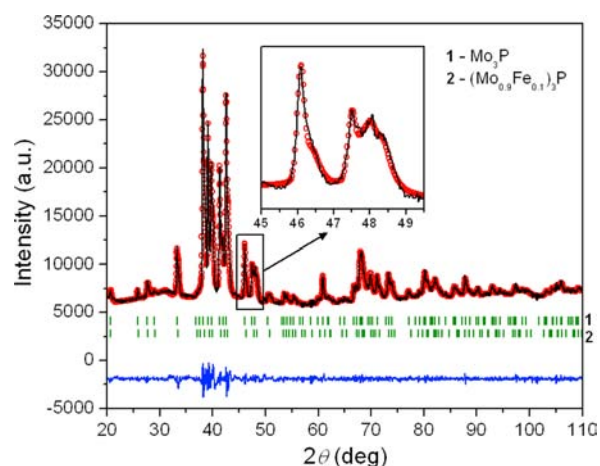

Figure 2. Powder XRD pattern for a two-phase sample containing Mo$_3$P and (Mo$_{0.90}$Fe$_{0.10}$)$_3$P. The calculated profile is indicated by circles and the observed profile by the solid line. Bragg peak positions are indicated by the tic marks (**1**, Mo$_3$P; **2**, (Mo$_{0.90}$Fe$_{0.10}$)$_3$P). The difference plot is shown at the bottom. The inset highlights the splitting of peaks attributable to the presence of the two phases.

Table 1. Crystallographic Data for Mo$_3$P and (Mo$_{0.90}$Fe$_{0.10}$)$_3$P from Powder X-ray Diffraction

	Mo$_3$P	(Mo$_{0.90}$Fe$_{0.10}$)$_3$P
formula mass (amu)	318.79	306.77
space group	$I\bar{4}2m$ (no. 121)	$I\bar{4}$ (no. 82)
a (Å)	9.752(1)	9.690(1)
c (Å)	4.792(1)	4.767(1)
V (Å^3)	455.8(1)	447.5(1)
Z	8	8
ρ_{calcd} (g cm^{-3})	9.292	9.106
diffractometer	Inel CPS-120	
radiation	Cu Kα_1, λ = 1.54056 Å	
2θ range (deg)	20.00–113.00	
step width (deg)	0.029	
no. of parameters	15	20
$B_{overall}$ (Å^2)	0.2(1)	0.9(1)
phase fraction	0.21(1)	0.79(3)
$R_B{}^a$	0.074	0.034
$R_F{}^b$	0.053	0.028
$R_p{}^c$		0.021

$^a R_B = \Sigma|I_o - I_c|/\Sigma|I_o|$. $^b R_F = \Sigma|F_o - F_c|/\Sigma|F_o|$. $^c R_p = \Sigma|y_o - y_c|/\Sigma y_o$.

these crystals were checked by EDX analyses. Within detection limits, no Fe was found in the Mo$_3$P crystal, whose composition (76(1)% Mo, 24(1)% P) agrees well with expected values (75% Mo, 25% P). The composition of the crystal of the ternary phase (62(1)% Mo, 13(1)% Fe, 25(1)% P) is reasonably close to the upper limit of Fe substitution (64% Mo, 11% Fe, 25% P). Intensity data were collected at −100 °C on a Bruker D8 diffractometer equipped with a SMART APEX II CCD area detector and a Mo Kα radiation source, using ω scans at seven different ϕ angles with a frame width of 0.3° and an exposure time of 12–15 s per frame. Face-indexed numerical absorption corrections were applied. Structure solution and refinement were carried out with use of the SHELXTL (version 6.12) program package.[20] Although the tetragonal cell parameters for two crystals are similar, inspection of the $hk0$ nets clearly reveals different Laue

symmetries, $4/mmm$ for Mo$_3$P vs $4/m$ for (Mo$_{0.85}$Fe$_{0.15}$)$_3$P (Figure S2 in the Supporting Information). For Mo$_3$P, the noncentrosymmetric space group $I\bar{4}2m$ was chosen; initial positions for all atoms were easily located by direct methods; and refinements proceeded in a straightforward manner in accordance with the α-V$_3$S-type structure.[21] For (Mo$_{0.85}$Fe$_{0.15}$)$_3$P, the noncentrosymmetric space group $I\bar{4}$ was chosen, and the model suggested by direct methods was consistent with the Ni$_3$P-type structure.[22] If all three metal sites were occupied by Mo atoms, one of them had unusually large displacement parameters, suggesting that it is disordered with Fe atoms. Refinements were conducted in which Mo and Fe atoms were allowed to disorder successively over each of the three metal sites. The first two sites contain exclusively Mo atoms (refined occupancies of 1.00(2)− 1.04(2) Mo and 0.00(2) Fe), whereas the third site contains a statistical mixture of both atoms (refined occupancies of 0.56(1) Mo and 0.44(1) Fe), with reasonable displacement parameters. The corresponding formula, Mo$_{2.56(1)}$Fe$_{0.44(1)}$P or (Mo$_{0.85(1)}$Fe$_{0.15(1)}$)$_3$P, matches precisely with the upper limit of Fe substitution in (Mo$_{1-x}$Fe$_x$)$_3$P. Table 2 summarizes crystallographic details of these refinements.

Atomic positions for Mo$_3$P, (Mo$_{0.90}$Fe$_{0.10}$)$_3$P, and (Mo$_{0.85}$Fe$_{0.15}$)$_3$P, which were standardized with the program STRUCTURE TIDY,[23] are listed in Table 3. Selected interatomic distances for Mo$_3$P and (Mo$_{0.85}$Fe$_{0.15}$)$_3$P are listed in Table 4. Further data for Mo$_3$P and (Mo$_{0.85}$Fe$_{0.15}$)$_3$P, in the form of crystallographic information files (CIFs), are available as Supporting Information or may be obtained from Fachinformationszentrum Karlsruhe, Abt. PROKA, 76344 Eggenstein-Leopoldshafen, Germany (CSD-425527 to 425528).

Band Structure Calculations. Tight-binding linear muffin tin orbital band structure calculations were performed within the local density and atomic spheres approximation with use of the Stuttgart TB-LMTO-ASA program (version 4.7).[24] For Mo$_3$P, the band structure was first evaluated for the observed crystal structure (α-V$_3$S-type, space group $I\bar{4}2m$) and then for hypothetical structures (Ni$_3$P-type, space group $I\bar{4}$) in which groupings of fused triangles are gradually rotated in increments of 2° relative to the undistorted structure. For (Mo$_{1-x}$Fe$_x$)$_3$P, a model was considered based on the composition "Mo$_{2.5}$Fe$_{0.5}$P" (close to the Fe-rich limit of this phase, (Mo$_{0.85}$Fe$_{0.15}$)$_3$P), with an ordered distribution of Mo and Fe atoms in

Table 2. Crystallographic Data for Mo$_3$P and (Mo$_{0.85}$Fe$_{0.15}$)$_3$P from Single-Crystal X-ray Diffraction

	Mo$_3$P	(Mo$_{0.85(1)}$Fe$_{0.15(1)}$)$_3$P
formula mass (amu)	318.79	301.15
space group	$I\bar{4}2m$ (no. 121)	$I\bar{4}$ (no. 82)
a (Å)	9.7925(11)	9.6982(8)
c (Å)	4.8246(6)	4.7590(4)
V (Å^3)	462.65(9)	447.61(6)
Z	8	8
ρ_{calcd} (g cm^{-3})	9.154	8.938
T (K)	173(2)	173(2)
crystal dimensions (mm)	0.06 × 0.04 × 0.03	0.10 × 0.04 × 0.03
radiation	graphite monochromated Mo Kα, λ = 0.71073 Å	
μ(Mo Kα) (mm^{-1})	16.272	17.204
transmission factors	0.632−0.772	0.357−0.715
2θ range (deg)	5.88−66.26	5.94−66.24
data collected	$-14 \leq h \leq 14, -14 \leq k \leq 15, -7 \leq l \leq 7$	$-14 \leq h \leq 14, -14 \leq k \leq 14, -7 \leq l \leq 7$
no. of data collected	3388	3137
no. of unique data, including $F_o{}^2 < 0$	476 (R_{int} = 0.026)	834 (R_{int} = 0.027)
no. of unique data, with $F_o{}^2 > 2\sigma(F_o{}^2)$	461	793
no. of parameters	24	39
$R(F)$ for $F_o{}^2 > 2\sigma(F_o{}^2)^a$	0.015	0.018
$R_w(F_o{}^2)^b$	0.031	0.036
goodness of fit	1.13	1.09
$(\Delta\rho)_{max}, (\Delta\rho)_{min}$ (e Å^{-3})	0.89, −0.76	0.90, −0.80

$^a R(F) = \sum||F_o| - |F_c||/\sum|F_o|$. $^b R_w(F_o{}^2) = [\sum[w(F_o{}^2 - F_c{}^2)^2]/\sum w F_o{}^4]^{1/2}$; $w^{-1} = [\sigma^2(F_o{}^2) + (Ap)^2 + Bp]$, where $p = [\max(F_o{}^2,0) + 2F_c{}^2]/3$.

Table 3. Atomic Coordinates for Mo_3P, $(Mo_{0.90}Fe_{0.10})_3P$, and $(Mo_{0.85}Fe_{0.15})_3P$

atom	Wyckoff position	x	y	z	U_{eq} ($Å^2$)^a
		Mo_3P (single-crystal data)			
Mo1	8i	0.0926(1)	0.0926(1)	0.2662(1)	0.0032(1)
Mo2	8i	0.2987(1)	0.2987(1)	0.2664(1)	0.0032(1)
Mo3	8g	0.3550(1)	0	1/2	0.0029(1)
P	8f	0.2913(1)	0	0	0.0035(2)
		Mo_3P (powder data)^b			
Mo1	8i	0.095(1)	0.095(1)	0.268(2)	
Mo2	8i	0.297(1)	0.297(1)	0.264(2)	
Mo3	8g	0.353(1)	0	1/2	
P	8f	0.305(1)	0	0	
		$(Mo_{0.90}Fe_{0.10})_3P$ (powder data)^b			
Mo1	8g	0.079(1)	0.109(1)	0.248(2)	
Mo2	8g	0.140(1)	0.478(1)	0.023(3)	
Mo/Fe3^c	8g	0.318(1)	0.283(1)	0.221(2)	
P	8g	0.319(2)	0.027(3)	0.011(7)	
		$(Mo_{0.85}Fe_{0.15})_3P$ (single-crystal data)			
Mo1	8g	0.0819(1)	0.1036(1)	0.2623(1)	0.0070(1)
Mo2	8g	0.1433(1)	0.4749(1)	0.0048(1)	0.0084(1)
Mo/Fe3^d	8g	0.3226(1)	0.2803(1)	0.2480(1)	0.0084(1)
P	8g	0.2912(1)	0.0380(1)	0.0018(3)	0.0096(2)

$^a U_{eq}$ is defined as one-third of the trace of the orthogonalized U_{ij} tensor. ^{b}Displacement parameters for individual atoms were not refined. ^{c}Fixed occupancies of 0.70 Mo and 0.30 Fe. ^{d}Refined occupancies of 0.56(1) Mo and 0.44(1) Fe.

Table 4. Selected Interatomic Distances (Å) in Mo_3P and $(Mo_{0.85}Fe_{0.15})_3P^a$

Mo_3P			
Mo1−P (×2)	2.502(1)	Mo3−P (×2)	2.488(1)
Mo1−Mo1	2.564(1)	Mo3−P (×2)	2.492(1)
Mo1−Mo2	2.843(1)	Mo3−Mo2 (×2)	2.793(1)
Mo1−Mo2	2.844(1)	Mo3−Mo3	2.840(1)
Mo1−Mo2	2.855(1)	Mo3−Mo1 (×2)	2.949(1)
Mo1−Mo1 (×2)	2.894(1)	P−Mo2 (×2)	2.436(1)
Mo1−Mo3(×2)	2.949(1)	P−Mo3 (×2)	2.488(1)
Mo2−P (×2)	2.436(1)	P−Mo3 (×2)	2.492(1)
Mo2−Mo2 (×2)	2.764(1)	P−Mo3 (×2)	2.502(1)
Mo2−Mo3 (×2)	2.793(1)	P−Mo2 (×2)	3.196(1)
Mo2−Mo1	2.843(1)		
Mo2−Mo1	2.844(1)		
$(Mo_{0.85}Fe_{0.15})_3P$			
Mo1−P	2.462(1)	Mo/Fe3−P	2.404(1)
Mo1−P	2.498(1)	Mo/Fe3−P	2.643(1)
Mo1−Mo1	2.563(1)	Mo/Fe3−P	2.503(1)
Mo1−Mo/Fe3	2.732(1)	Mo/Fe3−Mo2	2.659(1)
Mo1−Mo/Fe3	2.848(1)	Mo/Fe3−Mo1	2.732(1)
Mo1−Mo2	2.886(1)	Mo/Fe3−Mo2	2.780(1)
Mo1−Mo/Fe3	2.896(1)	Mo/Fe3−Mo/Fe3 (×2)	2.827(1)
Mo1−Mo1 (×2)	2.898(1)	Mo/Fe3−Mo1	2.848(1)
Mo2−P	2.452(2)	P−Mo/Fe3	2.404(1)
Mo2−P	2.480(2)	P−Mo2	2.452(2)
Mo2−P	2.488(1)	P−Mo2	2.462(1)
Mo2−P	2.504(1)	P−Mo2	2.480(2)
Mo2−Mo/Fe3	2.659(1)	P−Mo2	2.488(1)
Mo2−Mo/Fe3	2.780(1)	P−Mo1	2.498(1)
Mo2−Mo/Fe3	2.815(1)	P−Mo/Fe3	2.503(1)
Mo2−Mo2	2.821(1)	P−Mo2	2.504(1)
Mo2−Mo1	2.886(1)	P−Mo/Fe3	2.643(1)

^{a}Evaluated from single-crystal data.

space group $I2$ and cell parameters of $a = c = 9.6982$ Å, $b = 4.7590$ Å, and $\beta = 90°$. A similar analysis was performed in which the structure is gradually twisted. Other ordered models were inspected in which Fe atoms were placed in the alternative metal sites to determine the site preference. The basis sets included Mo 4d/4f/5s/5p, Fe 3d/4s/4p, and P 3s/3p/3d orbitals, with the Mo 4f and P 3d orbitals being downfolded. Integrations in reciprocal space were carried out using a k-point mesh of $8 \times 8 \times 8$ with an improved tetrahedron method.

Electrical Resistivity. Crystals of $(Mo_{0.85}Fe_{0.15})_3P$, whose identities were verified by EDX analysis, were mounted for standard four-probe electrical resistivity measurements between 2 and 300 K on a Quantum Design Physical Property Measurement System (PPMS) equipped with an ac transport controller (model 7100). Silver paste (DuPont 4929N) was used as the contacting agent from the crystal to graphite fibers and gold wires. The current was 100 μA, and the frequency was 16 Hz. Measurements were repeated twice.

■ RESULTS AND DISCUSSION

Mo−Fe−P Phase Diagram. On the basis of the analysis (powder and single-crystal X-ray diffraction; metallography) of about 40 samples (including some duplicates to confirm reproducibility), the isothermal section of the Mo−Fe−P phase diagram at 800 °C was constructed in the range of 0−67 atom % P (Figure 3). Crystallographic data for binary and ternary phases observed under these conditions are summarized in Table 5.

Among binary phases, we confirmed the existence of Mo_3P (α-V_3S-type), Mo_4P_3 (own type), MoP (WC-type), and MoP_2 (own type) in the Mo−P system; Fe_3P (Ni_3P-type), Fe_2P (own type), FeP (MnP-type), and FeP_2 ($FeAs_2$-type) in the Fe−P system; and Mo_6Fe_7 (W_6Fe_7-type) and $MoFe_2$ ($MgZn_2$-type) in the Mo−Fe system. These results agree well with previous literature data.[25] A slight solubility of the third component in these binary phases was found in four cases: $Mo_{1-x}Fe_xP$ ($x = 0–0.07$), $Mo_{1-x}Fe_xP_2$ ($x = 0–0.10$), $(Mo_xFe_{1-x})_3P$ ($x = 0–0.07$), and $(Mo_xFe_{1-x})_2P$ ($x = 0–0.05$).

Among ternary phases, we did not observe the previously reported polyphosphide $MoFe_2P_{12}$, which appears to be thermodynamically stable only within a narrow temperature
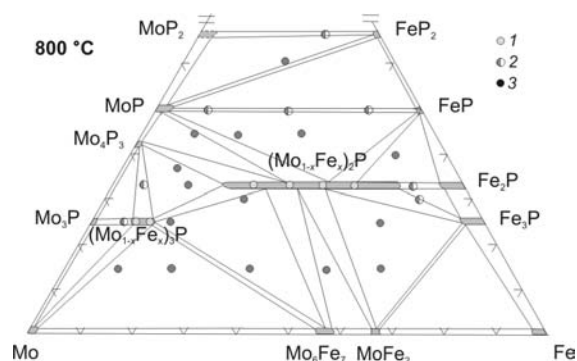
Figure 3. Isothermal section of the Mo−Fe−P phase diagram at 800 °C. The circles mark the location of samples containing one, two, or three phases as identified in the legend.

range centered around 700 °C and which was prepared in the presence of a Sn flux.[13] Its highly P-rich composition (80 atom % P) also lies well above the range investigated here. The equiatomic compound MoFeP has been reported previously to crystallize in the TiNiSi-type structure (a ternary ordered variant of the Co_2Si-type structure); a solid solution extending to Fe-rich compositions was also suggested.[12] Here, we have established that MoFeP belongs to a solid solution $(Mo_{1−x}Fe_x)_2P$ extending to both Mo- and Fe-rich compositions, with a rather broad homogeneity range ($x = 0.30−0.82$) in which Mo and Fe atoms would have to be disordered within the Co_2Si-type structure. The large solubility is somewhat surprising given that Mo and Fe are not particularly close in size (cf. metallic radii R_1 of 1.30 Å for Mo and 1.17 Å for Fe).[26] Presumably there would have to be some preferred occupation of the larger Mo vs smaller Fe atoms within the two available metal sites in the Co_2Si-type structure. The occurrence of an $(M_{1−x}M'_x)_2P$ phase with the Co_2Si-type structure is common to many other ternary transition-metal phosphide systems M−M'−P (where at least one metal M or M' is a 3d-metal).[27] Among the few exceptions are the Ti−Fe−P and Ti−Cr−P systems in which the $(M_{1−x}M'_x)_2P$ phase adopts an Fe_2P-type structure.[28,29] In this respect, the features found in the Mo−Fe−P system resemble those in related M−Fe−P systems (e.g., M = Nb, Zr, Re).[30−32]

A new ternary phase $(Mo_{1−x}Fe_x)_3P$ with a narrower homogeneity range ($x = 0.10−0.15$) was also identified. However, its composition and tetragonal cell parameters are close to those of the binary phase Mo_3P, raising questions on whether $(Mo_{1−x}Fe_x)_3P$ is truly a ternary phase. The Mo−Ni−P system poses the same problems in which an apparent ternary phase $(Mo_{0.9}Ni_{0.1})_3P$ is impossible to distinguish from the binary phase Mo_3P on the basis of their powder X-ray diffraction patterns.[11] These problems are exacerbated by the lack of an accurate structure determination of Mo_3P and discrepancies in the assignment of its structure type.[6−8] As now demonstrated by careful crystallographic analysis (vide supra), $(Mo_{1−x}Fe_x)_3P$ is indeed a bona fide ternary phase that is distinct from the binary phase Mo_3P.

Comparison of Mo_3P and $(Mo_{0.85}Fe_{0.15})_3P$. In vindication of the single-crystal photographic investigations by Sellberg and Rundqvist,[8] the present study confirms that Mo_3P adopts the α-V_3S-type structure (space group $I\bar{4}2m$) and not the Ni_3P-type structure (space group $I\bar{4}$) as suggested in earlier studies.[6] (The Ni_3P-type structure is synonymous with the Fe_3P-type structure, but we choose the former term because it is used in crystallographic databases.) In contrast, $(Mo_{1−x}Fe_x)_3P$ ($x = 0.10−0.15$) does adopt the lower-symmetry Ni_3P-type structure. The two types are part of a family of closely related structures adopted by many metal-rich phases M_3X (M = group 4 or 5 metal; X = B, Si, Ge, P, As, Sb, S).[33]

These structures can be very difficult to visualize. However, a good start is to focus on the stacking of nets, a principle that often works well for the structures of many intermetallic and metal-rich phases.[34] The structures of Mo_3P and $(Mo_{0.85}Fe_{0.15})_3P$ (the Fe-richest member of the solid solution $(Mo_{1−x}Fe_x)_3P$) are compared in Figure 4. Both are built up of nets stacked along the c-direction. The primary nets, located at $z = 1/4$ and $3/4$, consist of octagons and triangles of Mo atoms (or $[3^28^2][38^2]$ in Schläfli notation). These are interleaved by secondary nets, located at $z = 0$ and $1/2$, containing isolated Mo_2P_2 diamonds (or two fused triangles) which lie within the large channels concentric with the octagons in the primary nets. The nets undergo twisting along 4-fold rotation axes on proceeding from Mo_3P to $(Mo_{0.85}Fe_{0.15})_3P$, thereby eliminating mirror planes parallel to the c-direction. In the ternary phase, the Fe atoms preferentially occupy one of the Mo sites (at the $[38^2]$ nodes) within the primary nets. (Athough standardization

Table 5. Crystallographic Data for Phases in the Mo−Fe−P System[a]

phase	structure type	solubility	a (Å)	b (Å)	c (Å)
		binary and pseudobinary phases			
Mo_3P	α-V_3S ($I\bar{4}2m$)	negligible	9.798(2)		4.815(1)
Mo_4P_3	Mo_4P_3 (Pnma)	negligible	12.413(5)	3.159(1)	20.416(3)
MoP	WC ($P\bar{6}m2$)	0−4 atom % Fe ($Mo_{1−x}Fe_xP$; $x = 0−0.07$)	3.2230(2)[b]−3.2217(1)		3.1915(2)[b]−3.1908(2)
MoP_2	MoP_2 ($Cmc2_1$)	0−3 atom % Fe ($Mo_{1−x}Fe_xP_2$; $x = 0−0.10$)	3.1415(6)−3.140(1)	11.174(2)−11.157(3)	4.9793(8)−4.977(1)
Fe_3P	Ni_3P ($I\bar{4}$)	0−5 atom % Mo $[(Mo_xFe_{1−x})_3P; x = 0−0.07]$	9.107(5)[c]−9.118(6)		4.460(5)[c]−4.469(5)
Fe_2P	Fe_2P ($P\bar{6}2m$)	0−3 atom % Mo $[(Mo_xFe_{1−x})_2P; x = 0−0.05]$	5.8675(3)[d]−6.023(5)		3.4581(2)[d]−3.310(7)
FeP	MnP (Pnma)	negligible	5.192(2)	3.100(1)	5.788(2)
FeP_2	$FeAs_2$ (Pnnm)	negligible	4.970(1)	5.648(2)	2.7203(5)
Mo_6Fe_7	W_6Fe_7 ($R\bar{3}m$)	negligible	4.758(1)		25.55(1)
$MoFe_2$	$MgZn_2$ ($P6_3/mmc$)	negligible	4.720(2)		7.795(9)
		ternary phases			
$(Mo_{1−x}Fe_x)_3P$	Ni_3P ($I\bar{4}$)	7−11 atom % Fe ($x = 0.10−0.15$)	9.772(3)−9.686(2)		4.807(3)−4.760(2)
$(Mo_{1−x}Fe_x)_2P$	Co_2Si (Pnma)	20−55 atom % Fe ($x = 0.30−0.82$)	5.943(4)−5.813(2)	3.669(2)−3.607(2)	6.817(5)−6.683(3)

[a]Cell parameters are listed for the lowest and highest limit of solubilities of the third component. [b]Refs 16 and 17. [c]Ref 18. [d]Ref 15.
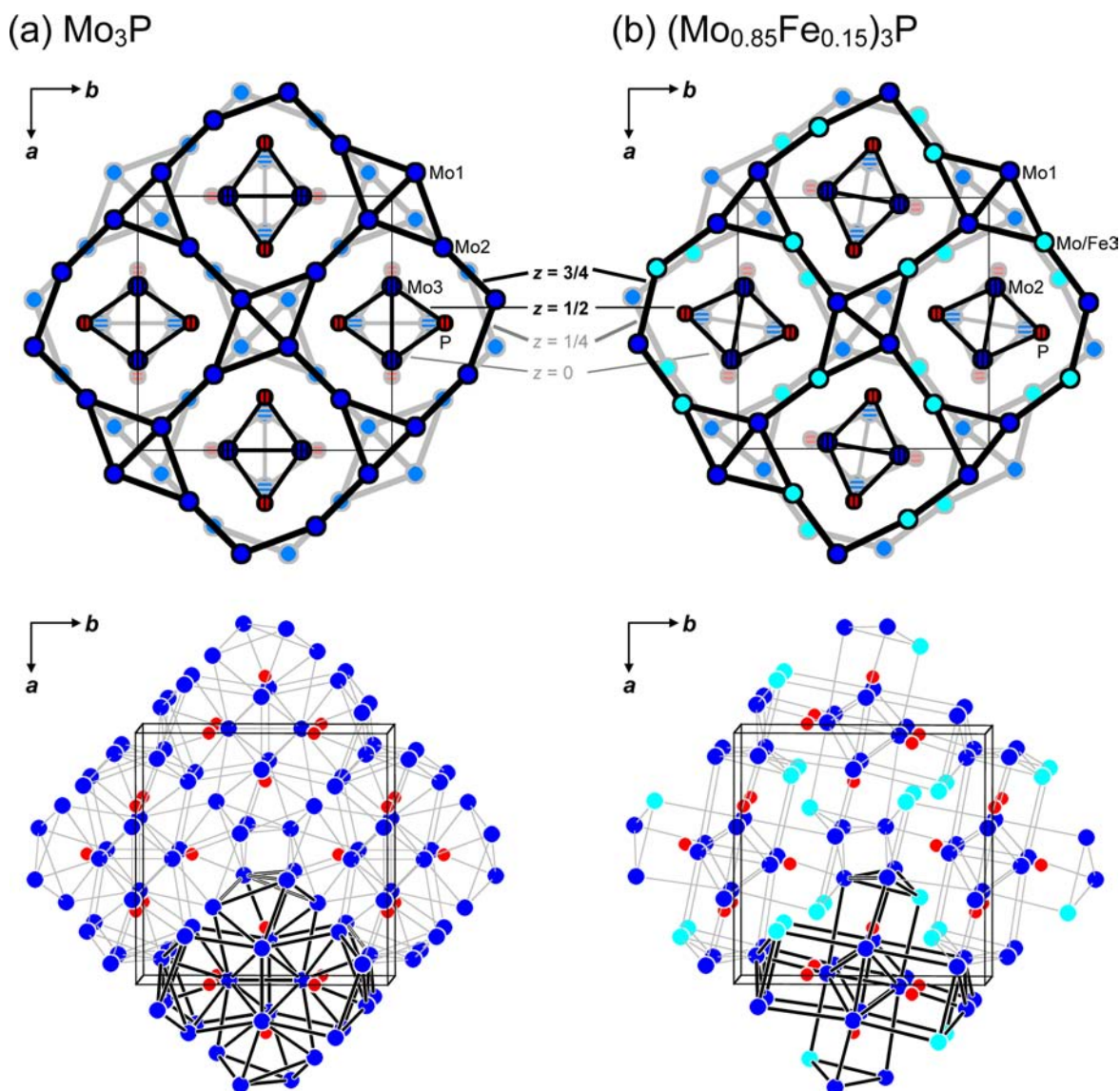
Figure 4. Structures of (a) Mo_3P and (b) $(Mo_{0.85}Fe_{0.15})_3P$ viewed down the c-direction, represented in terms of stacking of nets (top panels) or tetrameric assemblies of P-centered polyhedra (bottom panels).

of the crystallographic data unfortunately interchanges the identification of Mo2 and Mo3 in the two structures, we opt to retain the labeling nevertheless.)

The complicated connectivity of the three-dimensional framework is best visualized in terms of P-centered coordination polyhedra with metal atoms at the vertices. These are outlined in Figure 4, which highlights assemblies of tetrameric clusters that extend as columns down the c-direction. Surrounding an empty central tetrahedron are four square antiprisms in Mo_3P or four trigonal prisms in $(Mo_{0.85}Fe_{0.15})_3P$, as shown in Figure 5. In Mo_3P, the square antiprisms are distorted, with eight P−Mo distances in the range of 2.436(1)− 2.502(1) Å; two additional Mo atoms are located outside the square faces at much longer distances of 3.196(1) Å so that the coordination geometry could also be described as a bicapped square antiprism (CN8 + 2). In $(Mo_{0.85}Fe_{0.15})_3P$, three additional metal atoms are found outside the quadrilateral faces of the trigonal prisms so that the coordination geometry is properly described as a tricapped trigonal prism (CN9), with distances to the metal atoms in the range of 2.404(1)−

2.643(1), the shortest being to a mixed Mo/Fe3 site. The coordination geometries around the metal atoms are much more irregular (Figure S3 in Supporting Information). In general, the metal sites in Mo_3P and $(Mo_{0.85}Fe_{0.15})_3P$ could be described as being centered within distorted tetrahedra containing two, three, or four P atoms at the vertices (and metal atoms at the remaining vertices). However, the preponderance of metal−metal bonding (with a gradation of distances starting from as short as 2.563(1) Å) and the lack of a clear cutoff between nearest and next-nearest neighbors make it difficult to define coordination numbers and geometries.

Electronic Structure. Superficially, it may be thought that size factors could explain the evolution from the more symmetric structure of Mo_3P to the less symmetric one of $(Mo_{0.85}Fe_{0.15})_3P$ upon substitution with smaller Fe atoms, which would lead to a distortion to maintain appropriate distances to P atoms. However, as presaged by Rundqvist et al., who framed an argument in terms of the cohesive strength of transition metals to understand structural trends in M_3X compounds, the need to optimize metal−metal bonding
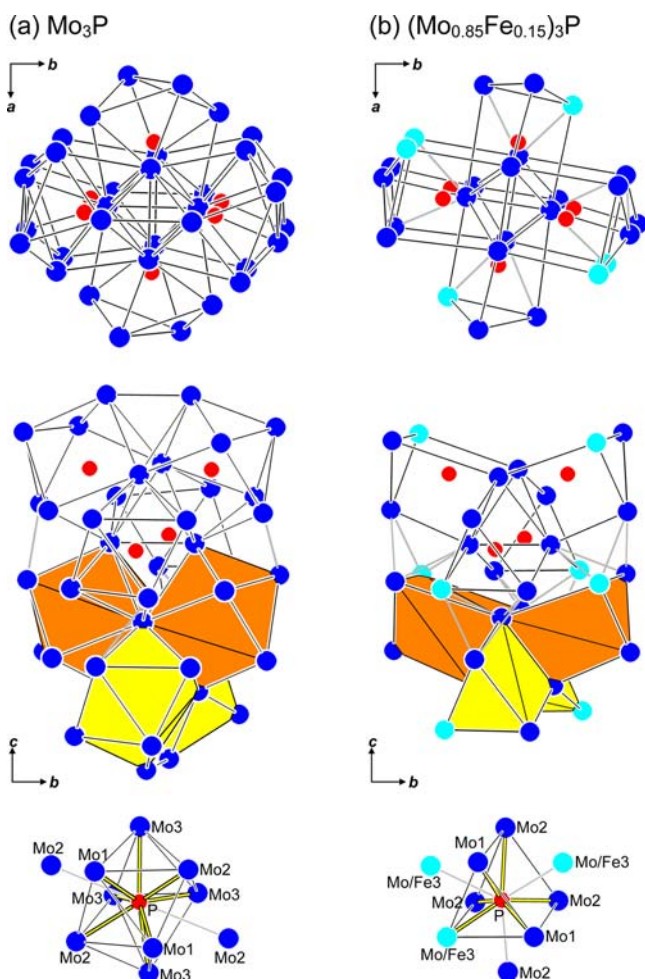
Figure 5. Tetrameric assemblies of P-centered polyhedra in (a) Mo_3P and (b) $(Mo_{0.85}Fe_{0.15})_3P$, viewed along (top panels) or normal to the c-direction (middle panels). An empty central tetrahedron is surrounded by four P-centered square antiprisms in Mo_3P or trigonal prisms in $(Mo_{0.85}Fe_{0.15})_3P$, as highlighted in the middle panels. The complete coordination polyhedra are actually bicapped square antiprisms (CN8 + 2) in Mo_3P or tricapped trigonal prisms (CN9) in $(Mo_{0.85}Fe_{0.15})_3P$ (bottom panels).

interactions is likely a more important consideration in stabilizing these metal-rich structures.[33] We have carried out band structure calculations to answer three questions: (i) Why does Mo_3P adopt the α-V_3S- and not the Ni_3P-type structure, and conversely why does $(Mo_{0.85}Fe_{0.15})_3P$ adopt the Ni_3P- and not the α-V_3S-type structure? (ii) What is the site preference of the Fe atoms in $(Mo_{0.85}Fe_{0.15})_3P$? (iii) Can $(Mo_{1-x}Fe_x)_3P$ with the Ni_3P-type structure be stable over a range of electron counts?

The description in terms of stackings of nets (Figure 4) provides a pathway to transform the α-V_3S- to the Ni_3P-type structure, through a twisting of the nets along the 4-fold rotation axes. The characteristic features common to these nets are groupings of fused triangles. For Mo_3P, these fused triangles ("Mo_4" in the primary nets and "Mo_2P_2" in the secondary nets) are aligned strictly parallel or at 45° to the a- and b-directions. Calculations were performed starting from this undistorted structure and then gradually rotating these fused triangles. The total energy increases upon introduction of such rotations (Figure 6(a)), implying that the undistorted structure is most stable, in support of experimental observations. For
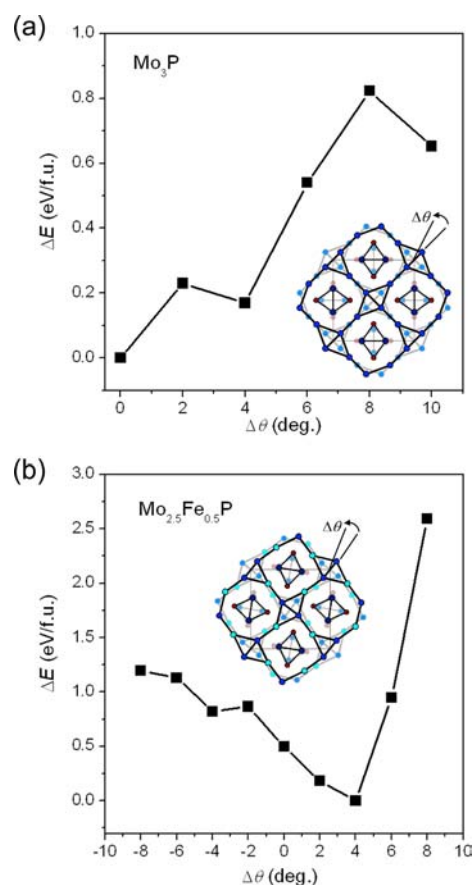

Figure 6. Relative energy as groupings of fused triangles are rotated by $\Delta\theta$ with respect to the undistorted structure in (a) Mo_3P or the initially distorted one in (b) $Mo_{2.5}Fe_{0.5}P$. (A negative rotation of about 8° in $Mo_{2.5}Fe_{0.5}P$ leads back to a nearly undistorted structure.)

$(Mo_{0.85}Fe_{0.15})_3P$, we analyzed models with the composition "$Mo_{2.5}Fe_{0.5}P$" (or "$Mo_{10}Fe_2P_4$" in the reduced unit cell) in which Fe atoms were placed in an ordered distribution within the originally disordered Mo/Fe3 site in the primary nets. If the initially distorted structure is rotated to reduce twisting, the total energy increases (Figure 6(b)). (A rotation of −8° renders the structure to be nearly undistorted, mimicking the α-V_3S-type structure.) In other words, "$Mo_{2.5}Fe_{0.5}P$" is more stable in the Ni_3P-type than the α-V_3S-type structure, in agreement with observation. If the structure is rotated to enhance twisting, the total energy actually falls slightly, but ultimately it rises very rapidly when the rotation is exacerbated.

In $(Mo_{0.85}Fe_{0.15})_3P$, there are three possible metal sites in which the Fe atoms could occupy. To avoid confusion with atom labels, we note these sites by their location within nets, the first two in the primary nets (at the $[38^2]$ or the $[3^28^2]$ nodes) and the third in the secondary nets. Calculations performed on different "$Mo_{2.5}Fe_{0.5}P$" models reveal that placement of Fe atoms within the $[38^2]$ nodes gives the lowest total energy, as observed. The energy increases by 0.20 eV/f.u. when Fe is placed in the $[3^28^2]$ nodes or by 0.32 eV/f.u. in the secondary nets.

It is anticipated that the electronic structures of these metal-rich compounds will be dominated by the metal atoms. The density of states (DOS) and crystal orbital Hamilton population (COHP) curves for Mo_3P bear out this expectation (Figure 7). The P-based states lie very deep in energy (5s at −13 to −12 eV; 5p at −7 to −5 eV). The Mo-based states
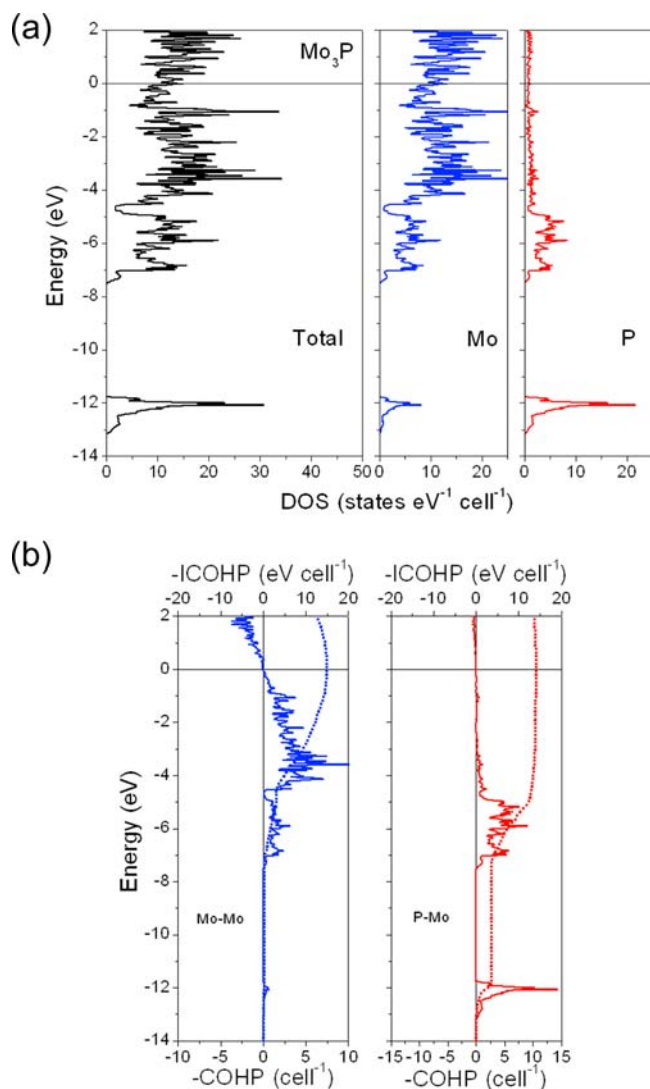
Figure 7. Mo₃P (α-V₃S-type): (a) Density of states (DOS) and its atomic projections. (b) Crystal orbital Hamilton population (−COHP) curves (solid lines) and integrated COHP (−ICOHP) curves (dotted lines) for Mo−Mo and P−Mo contacts. The Fermi level is at 0 eV.

Figure 8. Mo₂.₅Fe₀.₅P (Ni₃P-type): (a) Density of states (DOS) and its atomic projections. (b) Crystal orbital Hamilton population (−COHP) curves (solid lines) and integrated COHP (−ICOHP) curves (dotted lines) for metal−metal and P−metal contacts. The Fermi level is at 0 eV.

overlap with the P 5p states in the energy range from −7 to −5 eV to give rise to P−Mo bonding levels. Above −5 eV, the DOS is overwhelmingly of Mo 4d character, with Mo−Mo bonding being perfectly optimized and all bonding levels being just filled at the Fermi level. The results for "Mo₂.₅Fe₀.₅P" are similar except that Fe 3d states are now introduced and have an important contribution near the Fermi level (Figure 8). Moreover, Fe−Mo and Fe−Fe interactions are antibonding at the Fermi level, counteracting Mo−Mo bonding interactions. Decreasing the electron count alleviates the Fe−Mo antibonding interactions but at the expense of the Mo−Mo bonding interactions. However, the dependence of the integrated COHP values (−ICOHP) on changes in electron count is relatively weak near the Fermi level. The presence of a slight homogeneity range in (Mo₁₋ₓFeₓ)₃P may be attributed to this competition of Mo−Mo and Fe−Mo interactions. The observed phase width (x = 0.10−0.15) corresponds to adjusting the Fermi level within the range of −0.1 to 0 eV.

The absence of a band gap in the DOS curves implies metallic behavior, which is confirmed from the measurement of
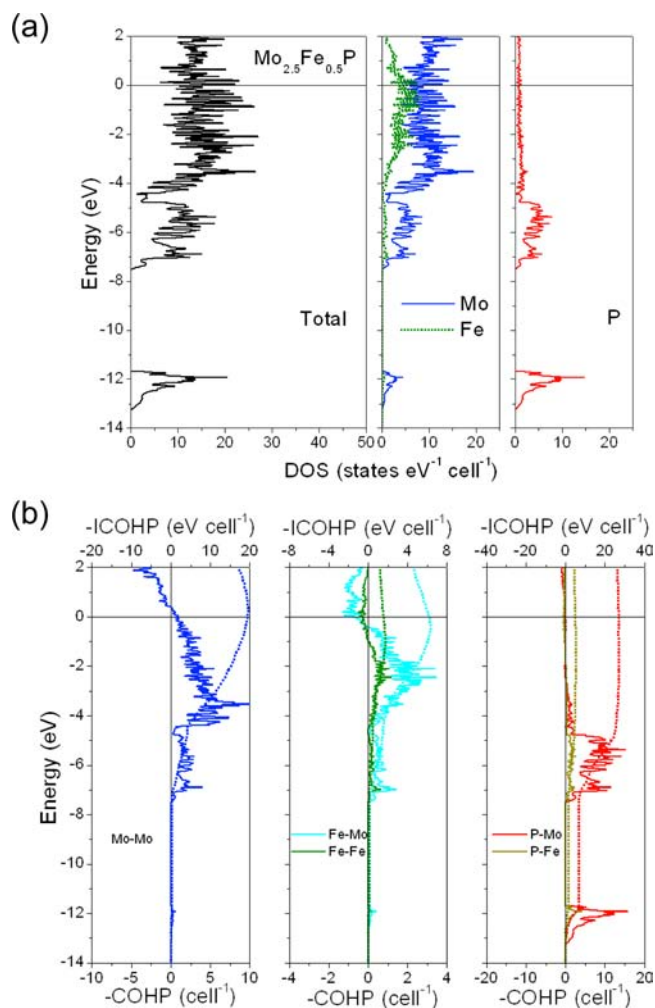
electrical resistivity of (Mo₀.₈₅Fe₀.₁₅)₃P (Figure 9). The temperature dependence shows a slightly concave down
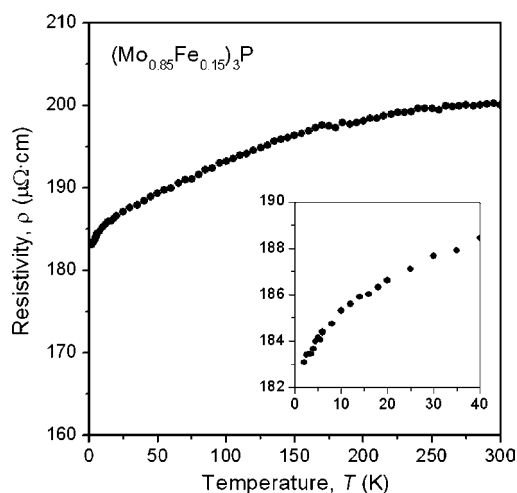
Figure 9. Plot of electrical resistivity vs temperature for (Mo₀.₈₅Fe₀.₁₅)₃P.

Article

curvature, and the resistivity appears to undergo a more rapid decrease below 10 K. The behavior resembles that of Mo_3P,[4] except that the superconducting transition at 7 K is suppressed. The absolute values of the resistivity (ρ_{300K} = 200 $\mu\Omega\cdot$cm) are similar to Mo_3P, and the small relative resistivity ratio (ρ_{300K}/ρ_{2K} = 1.1) is consistent with the presence of Mo/Fe disorder. As noted above, introduction of Fe atoms provides important contributions to the DOS at the Fermi level, which strongly influences electrical properties.

■ CONCLUSIONS

The Mo−Fe−P system is characterized by slight or negligible solubility of the third component in the binary phases and the existence of only two ternary phases, $(Mo_{1-x}Fe_x)_2P$ with a broad homogeneity range (x = 0.30−0.82) and $(Mo_{1-x}Fe_x)_3P$ with a narrow homogeneity range (x = 0.10−0.15). The ternary phase $(Mo_{1-x}Fe_x)_3P$ is distinct from the binary phase Mo_3P, even though their compositions and structures are similar. The introduction of Fe suppresses the superconducting transition that takes place in Mo_3P. The electronic structure of Mo_3P itself seems to be rather different from other related M_3X compounds, such as superconducting Nb_3Sn, for which sharp peaks near the Fermi level are found.[35,36] It is apparent that metal−metal bonding is indeed important in influencing the electronic properties in binary molybdenum phosphides, as anticipated earlier,[4,5] but the effects are more subtle than simply a correlation with bond distances.

■ ASSOCIATED CONTENT

Ⓢ Supporting Information
X-ray crystallographic files in CIF format, SEM image and EDX spectrum, X-ray diffraction patterns, and additional coordination polyhedra. This material is available free of charge via the Internet at http://pubs.acs.org.

■ AUTHOR INFORMATION

Corresponding Author
*E-mail: yalomnytska@yahoo.com (Y.F.L.); arthur.mar@ualberta.ca (A.M.).

Notes
The authors declare no competing financial interest.

■ ACKNOWLEDGMENTS

■ REFERENCES

(1) Oyama, S. T.; Gott, T.; Zhao, H.; Lee, Y.-K. *Catal. Today* **2009**, *143*, 94−107.
(2) Kamihara, Y.; Hiramatsu, H.; Hirano, M.; Kawamura, R.; Yanagi, H.; Kamiya, T.; Hosono, H. *J. Am. Chem. Soc.* **2006**, *128*, 10012−10013.
(3) Stewart, G. R. *Rev. Mod. Phys.* **2011**, *83*, 1589−1652.
(4) Shirotani, I.; Kaneko, I.; Takaya, M.; Sekine, C.; Yagi, T. *Physica B* **2000**, *281−282*, 1024−1025.
(5) Shirotani, I.; Takaya, M.; Kaneko, I.; Sekine, C.; Yagi, T. *Physica C* **2001**, *357−360*, 329−332.
(6) Schönberg, N. *Acta Chem. Scand.* **1954**, *8*, 226−239.
(7) Rundqvist, S.; Lundström, T. *Acta Chem. Scand.* **1963**, *17*, 37−46.
(8) Sellberg, B.; Rundqvist, S. *Acta Chem. Scand.* **1965**, *19*, 760−762.
(9) Lomnytska, Ya. F.; Chykhrij, S. I.; Kuz'ma, Yu. B. *J. Alloys Compd.* **2001**, *321*, 91−96.
(10) Vogel, R.; Hortmann, D. *Arch. Eisenhuettenwes.* **1953**, *24*, 369−374.
(11) Oryshchyn, S. V.; Le Sénéchal, C.; Députier, S.; Bauer, J.; Guérin, R.; Akselrud, L. G. *J. Solid State Chem.* **2001**, *160*, 156−166.
(12) Guérin, R.; Sergent, M. *Mater. Res. Bull.* **1977**, *12*, 381−388.
(13) Flörke, U.; Jeitschko, W. *Inorg. Chem.* **1983**, *22*, 1736−1739.
(14) Akselrud, L. G.; Grin, Yu. N.; Zavalij, P. Yu.; Pecharsky, V. K.; Fundamenskii, V. S. *Abstracts of Papers*, 12th European Crystallographic Meeting, Moscow, USSR, Aug 20−29, 1989.
(15) Rundqvist, S. *Acta Chem. Scand.* **1962**, *16*, 1−19.
(16) Andersson, M. *J. Alloys Compd.* **1993**, *198*, L15−L18.
(17) Fjellvåg, H.; Kjekshus, A. *Acta Chem. Scand., Ser. A* **1985**, *39*, 199−207.
(18) Artigas, M.; Bacmann, M.; Fruchart, D.; Wolfers, P.; Fruchart, R. *J. Alloys Compd.* **1991**, *176*, 105−114.
(19) Rodríguez-Carvajal, J. *FULLPROF*, version 4.80; Laboratoire Léon-Brillouin (CEA-CNRS): Saclay, France, 2001.
(20) Sheldrick, G. M. *SHELXTL*, version 6.12; Bruker AXS Inc.: Madison, WI, 2001.
(21) Pedersen, B.; Grønvold, F. *Acta Crystallogr.* **1959**, *12*, 1022−1027.
(22) Rundqvist, S.; Hassler, E.; Lundvik, L. *Acta Chem. Scand.* **1962**, *16*, 242−243.
(23) Gelato, L. M.; Parthé, E. *J. Appl. Crystallogr.* **1987**, *20*, 139−143.
(24) Tank, R.; Jepsen, O.; Burkhardt, A.; Andersen, O. K. *TB-LMTO-ASA Program*, version 4.7; Max Planck Institut für Festkörperforschung: Stuttgart, Germany, 1998.
(25) Villars, P.; Cenzual, K. *Pearson's Crystal Data — Crystal Structure Database for Inorganic Compounds*, release 2010/11; ASM International: Materials Park, OH, 2010.
(26) Pauling, L. *The Nature of the Chemical Bond*, 3rd ed.; Cornell University Press: Ithaca, NY, 1960.
(27) Lomnytska, Ya. F.; Kuz'ma, Yu. B. *J. Alloys Compd.* **1998**, *269*, 133−137.
(28) Ivanov, A. V.; Zolensky, M. E.; Saito, A.; Ohsumi, K.; Yang, S. V.; Kononkova, N. N.; Mikouchi, T. *Am. Mineral.* **2000**, *85*, 1082−1086.
(29) Babizhetskii, V. S.; Lomnitskaya, Ya. F. *Inorg. Mater. (Engl. Transl.)* **2002**, *38*, 905−906; *Neorg. Mater.* **2002**, *38*, 1077−1078.
(30) Lomnytska, Ya.; Myhalyna, M.; Toma, O. *Visn. Lviv. Univ. Ser. Khim.* **2011**, *52*, 14−21.
(31) Lomnytska, Ya.; Lata, M. *Visn. Lviv. Univ. Ser. Khim.* **2006**, *47*, 12−17.
(32) Oryshchyn, S. V.; Kuz'ma, Yu. B.; Terelyetskiy, R. M.; Dankevich, Yu. G. *Issled. Primen. Splavov Tugoplavkikh Met.* **1983**, 11−15.
(33) Rundqvist, S.; Andersson, Y.; Pramatus, S. *J. Solid State Chem.* **1979**, *28*, 41−49.
(34) Pearson, W. B. *The Crystal Chemistry and Physics of Metals and Alloys*; Wiley: New York, 1972.
(35) Mattheiss, L. F.; Weber, W. *Phys. Rev. B* **1982**, *25*, 2248−2269.
(36) Weber, W.; Mattheiss, L. F. *Phys. Rev. B* **1982**, *25*, 2270−2284.